**Final Scientific/Technical Report – DOE BTO BENEFIT Program**

| | |
|---|---|
| **Title:** | **Bio-Based Phase Change Materials (PCMs) for Thermal Energy Storage** |
| **Project Period:** | 04/01/20 – 03/31/22 |
| **Extension Period:** | 04/01/22 – 10/31/22 |
| **Submission Date:** | 03/30/2023 |
| **Recipient:** | Rector & Visitors of the University of Virginia |
| **Address:** | 210 Sprigg Ln.<br>Charlottesville, VA 22903 |
| **Website (if available)** | bov.virginia.edu |
| **Award Number:** | DE-EE0009157 |
| **Project Team:** | Experiments and Simulations in Thermal Engineering (ExSiTE) Lab, University of Virginia |
| **Principal Investigator:** | Patrick E. Hopkins, Professor<br>Phone: 434-982-6005<br>Email: phopkins@virginia.edu |
| **Business Contact:** | Stewart P. Craig<br>Phone: 434-924-4270<br>Email: ospnoa@virginia.edu |
| **HQ Tech Manager:** | Sven Mumme |
| **NETL Project Officer:** | Coriana Fitz |

This material is based upon work supported by the U.S. Department of Energy's Office of Energy Efficiency and Renewable Energy (EERE) under the BTO's BENEFIT Program, award number(s) DE-EE0009157. This report was prepared as an account of work sponsored by an agency of the United States Government. Neither the United States Government nor any agency thereof, nor any of its employees, makes any warranty, express or implied, or assumes any legal liability or responsibility for the accuracy, completeness, or usefulness of any information, apparatus, product, or process disclosed, or represents that its use would not infringe privately owned rights. Reference herein to any specific commercial product, process, or service by trade name, trademark, manufacturer, or otherwise does not necessarily constitute or imply its endorsement, recommendation, or favoring by the United States Government or any agency thereof. The views and opinions of authors expressed herein do not necessarily state or reflect those of the United States Government or any agency thereof.

**Abstract**

The goal of this project is to develop a novel bio-based phase change material (PCM) derived from squid ring teeth (SRT) proteins, and design a prototype heat exchanger based on these bio-based PCMs for energy storage and dynamic heat exchange for building thermal energy storage systems. The PCMs, derived from SRT proteins, will demonstrate room temperature energy storage capacities and switchable thermal conductivities that redefine the current state-of-the-art (SOA) for building thermal energy storage. Further, in a single material and with a single manufacturing processes, our proposed thermal battery will be developed with "on demand" thermal conductivity for rapid charging/discharging but superior insulation during energy storage periods. More specifically, our bio-based PCMs have demonstrated: 1) the potential for increased energy storage capacity (i.e., greater than paraffines at room temperature); 2) tunability in thermal conductivity with the largest thermal conductivity switching ratios for an intrinsic material reported to date, and 3) a 100% recyclable and biodegradable PCM with low volatility and toxicity and scalability in its manufacture for both residential and commercial applications. The already established ability for roll-to-roll processing of these non-toxic, non-flammable SRT composites along with their carbon-neutral manufacturing processes that has been pioneered by our team make this solution a disruptive and impactful technology to redefine the current SOA of energy storage technologies.

The outcomes of this effort have been: 1) the identification of new bio-based PCM that establishes a new SOA for thermal conductivity and energy storage density at room temperature and 2) the development of a new experimental technique to measure the energy storage density via latent heat measurements during melting of thin films. This new technique can be applied to thin films (as thin as < 1 micrometer), and represents a novel approach for thin film energy storage density measurements.

Dynamic thermal energy storage is the missing technology that will enable a grid-interactive efficient building (GEB). For a "smart" building capable of connecting with the power grid, the media must be inexpensive and possess thermal switching capabilities to control the time-dependent heat flow into (and out of) the PCM on demand. Unique to the material system in this program, programmable SRT-based PCM show improvements as compared to traditionally used PCMs, and thus its technical performance will represent a leap forward for the future GEB concept.

## i. Review of objectives

### Overarching Objective in Budget Period 1

The recipient will scale up production of SRT-based PCMs; demonstrate switchable thermal conductivities and increased energy storage capacities of SRT-based PCMs via thermal conductivity and heat capacity measurements; and perform thermodynamic and techno-economic analysis of thermal switching and thermal storage concepts.

### Milestone and Accomplishment Summary Table for Budget Period 1

| Task | Title | Description | Verification | Quarter | Status |
|---|---|---|---|---|---|
| 1.1 | Project Kick-Off and IPMP | Attend kick-off meeting and IP plan | Slides submitted at kick-off | 1 | Complete |
| 1.2 | Scale up SRT-based PCM | Scale-up SRT-based PCM to >0.5 kg with >80% purity and yield of 1 g/L | Quantity and purity | 3 | Complete |
| 1.3.1 | Tunable thermal cond. of SRT PCM | Tunable thermal cond. >1 W/m-K with switching ratios > 4x, and durability of >75% over 100 cycles | Thermal cond. measurements | 3 | Complete |
| 1.3.2 | Increased energy storage of hydrated SRT PCM | Energy density of at least 30 kWh $m^{-3}$, and durability of >75% over 100 cycles. | Composition and heat capacity measurements | 4 | Complete |
| 1.4 | Technoeconomic analysis of SRT PCM concepts | Evaluate system concepts to achieve system cost of $15/kWh at the 250,000 L scale utilizing SRT PCM. | Techno-economic analysis | 4 | Complete |

### Go/No-Go Table for Budget Period 1

| Related Task | Go/No-Go Milestones | Status at end of Q4 | Projected status at end of Budget Period 1 and notes |
|---|---|---|---|
| 1.2 | Synthesize 0.5 kg of SRT-based PCM at >80% purity and with a yield of >1 g/L | Complete | Complete |
| 1.3.1 | Achieve thermal conductivities >1 W $m^{-1}$ $K^{-1}$, switching ratios >4x | Complete | Complete |
| 1.3.2 | Demonstrate energy storage densities of energy storage densities > 30 kWhr $m^{-3}$ | Complete | Complete |
| 1.3.1 and 1.3.2 | Thermal conductivity and energy storage durability of >75% over 100 cycles. | Complete | Complete |

## Y2 Milestones/End of Project Goals

| Task Number | Milestone Description | Anticipated Months from Start of the Project | Anticipated Quarters from Start of the Project | Milestone Achieved (Y/N) |
|---|---|---|---|---|
| 2.1.1 | Determine SRT-based PCM plasticizing liquids to achieve $k_{max}/k_{min}$ = 8x with 75% durability over 500 cycles. Demonstrate hydrated thermal conductivities tunable from 0.25+/- 0.05 W $m^{-1}$ $K^{-1}$ to >1.6 W $m^{-1}$ $K^{-1}$ with >75% durability over 500 cycles. Determine how this degree of tunability changes based on % hydration, and study different plasticizing liquids. Thermal conductivity switching speed will be monitored and correlated to the size of the samples. | 19 | 7 | Y |
| 2.1.2 | Determine energy storage density of SRT-PCM samples ambient, fully hydrated, and partially hydrated states, and demonstrate energy storage densities of >100 kWhr $m^{-3}$ with > 75% durability over 500 cycles. Determine how this energy storage density changes based on % hydration of different plasticizing liquids. Stretch target of storage densities of >200 kWhr $m^{-3}$ with > 90% durability over 500 cycles. | 23 | 8 | Y |
| 2.2 | Perform component modeling/analysis and psychrometric analysis to quantify the benefits of SRT-PCM thermal switching for the built environment | 23 | 8 | Y |
| 2.3 | Scale-up SRT-based PCM to >1 kg with manufacturing plan to achieve >10 kg with >80% purity at a yield of 5 g/L (stretch target > 10 g/L). Refine cost model to inform improvement strategies. | 23 | 8 | Y |

**Program targets: All minimum targets met during this program**

| Description | Minimum Targets | Stretch Targets |
|---|---|---|
| **Phase Change Temperature** | Near room temperature demonstration | Room temperature, or tunable near room temperature depending on operating temperature of residential or commercial application |
| **System Cost** | <$15/kWh projected at 250,000 L volumetric fermentation scale | $13.50/kWh projected at 250,000 L volumetric fermentation scale |
| **Energy Density** | >100 kWh/$m^3$ | 200 kWh/$m^3$ |
| **Thermal Conductivity** | Tunable from 0.25+/- 0.05 W $m^{-1}$ $K^{-1}$ to >1.6 W $m^{-1}$ $K^{-1}$ | Tunable from 0.2 – 2.0 W $m^{-1}$ $K^{-1}$ |
| **Thermal Reliability** | >75% after 500 cycles | >90% after >5000 cycles |
| **Safety** | Non-toxic, non-flammable, non-explosive, and non-reactive | Non-toxic, non-flammable, non-explosive, and non-reactive |
| **Corrosion** | Non-corrosive | Non-corrosive and compatible with other materials in single manufacturing process |

## ii. Significant findings, conclusions, and developments

### ii.a. Squid ring teeth (SRT) PCM synthesis

**PCM-protein production:** Over the course of the project, we made good progress toward the end-of-project goal of 1 kg PCM-protein production. The total PCM-protein produced based on six 100-L bioreactor runs (Table 1) and 19 purifications (Table 2) was 635 g. The first four runs used the same protocol and achieve approximately 1 g/L volumetric yield, while the final two runs used a longer incubation time and achieved a higher volumetric yield of approximately 1.5 g/L due to a greater production of biomass. The bioreactor process was consistent from run to run, with wet biomass of approximately 1700 g (short run) and 3400 g (long run) produced per run. Likewise, the purification process was consistent as well, with yields of approximately 0.2 g (short run) and 0.15 g (long run) of protein produced per g of input dry biomass. Notably, no large-scale bioreactor run failed, and the only major purification failure was a human error in the final purification from batch TDR136. Our experiences suggest that we can reliably achieve a yield of 1.5 g/L when running at the 100-L scale making protein batches of 100 g and provide confidence that further scaleup is possible.

***Table 1: Summary of all six 100-L bioreactor batches performed for this project and associated PCM-protein purifications. Most of the biomass produced in each batch was used for purifications, except for TDR136, for which approximately half of the biomass was lost due to human error. Full-scale Yield: g of dry protein obtained per g of input dry biomass, based on representative large-scale purification results (Table T2). Volumetric yield (g/L): g of dry protein obtained per L of culture, based on the full-scale yield and total wet cell mass produced.***

| Batch | 100-L run sequence | Wet cell mass (g) | Dry cell mass used (g) | Dry Protein Produced (g) | Full-scale Yield | Volumetric yield (g/L) |
|---|---|---|---|---|---|---|
| TDR114 | 1 | 1757 | 560 | 124 | 0.22 | 1.23 |
| TDR118 | 2 | 1442 | 525 | 108 | 0.20 | 0.89 |
| TDR123 | 3 | 1931 | 562 | 101 | 0.177 | 1.07 |
| TDR128 | 4 | 1832 | 530 | 115 | 0.185 | 1.07 |
| TDR133 | 5 | 3468 | 960 | 109 | 0.135 | 1.48 |
| TDR136 | 6 | 3310 | 540 | 79 | 0.15 | 1.53 |

The primary impediment to greater production during the project was lack of availability of suitably large bioreactors at the CSL Behring fermentation facility we used. Although we ran the 100-L bioreactor at every available opportunity, a variety of issues limited this to six total runs: a slow start due to COVID-related facility closures at the beginning of the project, several facility closures due to phage contamination, high subscription of shared-use equipment due to COVID-related projects, and equipment breakdown that prevented us from running at 100-L scale. Furthermore, supply-chain and other issues limited final installation of a 500-L reactor we had expected to use during the project. Notably, the directors of the facility and their employees went above and beyond to help us in our

efforts to produce protein in the face of these issues; our achievements in this project would have been impossible without their continued assistance.

***Table 2: Data for all PCM-protein purification runs performed using the biomass from the six 100-L bioreactor batches. Batches TDR114 and TDR128 were processed as two serial extractions from biomass into DMSO; the yield from each extraction is given separately. Yield: g of dry protein obtained per g of input dry biomass for each purification. Full-scale yield: the yield achieved for the largest-scale purification from each batch, or the average of representative purifications. For TDR114 and TDR128, the full-scale yield is the sum of yields achieved from two serial purifications. For TDR133 and TDR136, the full-scale yield is the average yield of two equivalent large-scale purifications with slightly different conditions.***

| Batch | Purification | Dry cell input (g) | Output (g) | Yield | Full-scale yield |
|---|---|---|---|---|---|
| TDR114 | 8DH24 | 560 | 98 | 0.18 | 0.22 |
| | 8DH24-2 | | 26 | 0.05 | |
| TDR118 | 8DHF2 | 60 | 14 | 0.23 | |
| | 8DHF2-2 | | 3 | 0.05 | |
| | 8DHF3 | 465 | 70 | 0.15 | 0.20 |
| | 8DHF3-2 | | 22 | 0.05 | |
| TDR123 | 8DHF4 | 60 | 6 | 0.10 | |
| | 8DHF5 | 60 | 12 | 0.20 | |
| | 8DHF6 | 60 | 15 | 0.25 | |
| | 8DHF7 | 382 | 68 | 0.18 | 0.177 |
| TDR128 | 8DHF8 | 60 | 18 | 0.29 | |
| | 8DHF9 | 100 | 25 | 0.25 | |
| | 8DEF1 | 100 | 22 | 0.22 | |
| | 8DEF2 | 270 | 50 | 0.19 | 0.19 |
| TDR133 | 8DEF3 | 330 | 45 | 0.14 | 0.14 |
| | 8DEF4 | 300 | 40 | 0.13 | |
| | 8DHF11 | 330 | 23 | 0.07 | |
| TDR136 | 8DEF5 | 270 | 40 | 0.15 | 0.15 |
| | 8DEF6 | 270 | 39 | 0.14 | |
| Total | | 3677 | 635 | | |

**Yield:** As described in the previous section, volumetric yield of PCM protein TR8n8 as expressed from BL21(DE3)/pET-14b appears to max out at 1.5 g/L, with genetic instability and PCM protein toxicity the most likely culprits in this limitation. To address both of these potential issues, we developed a tightly repressed expression vector for PCM protein TR8n8 and applied it in a variety media formulations to identify conditions that allow higher biomass accumulation with protein production. We found that a defined minimal salts medium, with glucose and lactose to enable autoinduction of PCM-protein expression, allowed an improvement of nearly 2x in biomass yield relative to the baseline, with protein expression maintained.

When we repeated a run with the best media formulation found previously (D5.0), the biomass yield was somewhat lower than before (D5.0-repeat), but still substantially higher than the baseline performance of 18 g wet biomass / L achieved using 4xLB with 1% glycerol (Figure 1), and with good evidence of protein expression (Figure 2). When we attempted to use the same media formulation with the original, non-repressed expression vector (D5.0-pET-14b), the biomass yield was somewhat lower. Furthermore, protein expression declined over the course of the run, suggesting greater genetic instability of the first-generation construct. This result suggests that the rightly repressed vector, pBA407, is working as intended to bolster genetic stability and should be preferred.

We tried the best-performing formulation and process at the 50-L scale. Although the growth rate and protein expression were as expected, the run ended prematurely due to facility limitations (48 h total run time, compared to 66 h for equivalent runs at 5 L scale). Therefore, the total biomass produced was low. Based on the results of the truncated run, we have every reason to believe that a full-length run at the 50-L or 100-L scale would perform similarly to the 5-L scale.

Finally, we performed several runs with modified glucose concentrations to probe the effects of autoinduction timing on biomass production and protein expression. Condition D5.0A, in which the glucose concentration was lowered from 0.5% to 0.2%, is expected to begin induction earlier in the growth curve, while condition D5.0B (glucose = 0.8%), is expected to induce later. Preliminary results suggest that the higher-glucose condition expressed protein well but produced lower biomass, while the lower-glucose variant produced more biomass, contrary to our initial expectations. This suggests that the nutrient balance in this high-sugar media will need to be carefully tuned to support maximum biomass production, and potentially that slower growth with less glucose and a denser inoculum may be appropriate.

Although our validated volumetric yields at scale of 1.5 g/L fall short of the project end goal of 5 g/L, we anticipate that continued work with defined media and tightly repressed expression will achieve 2.5-3.0 g/L. Combined with screening of less toxic sequences (see sections below), target yields of 5 g/L should be possible as the groundwork laid during this project pays off as our development of the technology continues.

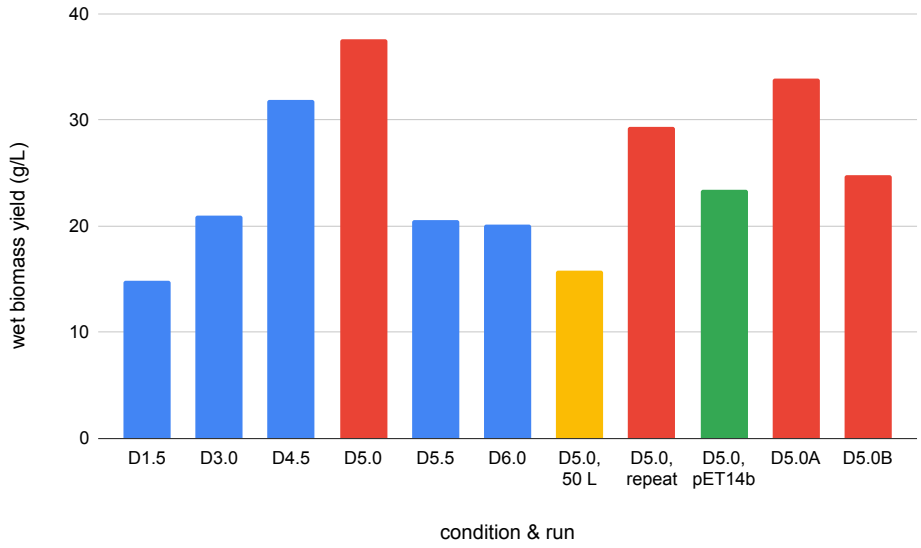


***Figure 1. Wet biomass yield per liter of culture for a variety of bioreactor runs using various defined media with autoinduction. All experiments use strain pBA407/BI21(DE3) to produce biomass and TR8n8 PCM protein in a 5-L bioreactor, and Studier N5052 media with glycerol, glucose, and lactose at a fixed mass ratio of 10:1:4, unless otherwise indicated. The number in the formulation name reflect the weight percent of glycerol in the media (Sugar1.5 has 1.5% glycerol, 0.15% glucose, and 0.6% lactose). D5.0 (red bars) reflects the best media formulation identified so far. D5.0A uses a reduced glucose concentration of 0.2%. D5.0B uses an increased glucose concentration of 0.8%. The green bar labelled pET-14b uses the original, non-repressed version of the TR8n8 expression vector. The gold bar labelled "50 L" is a 50-L bioreactor run.***

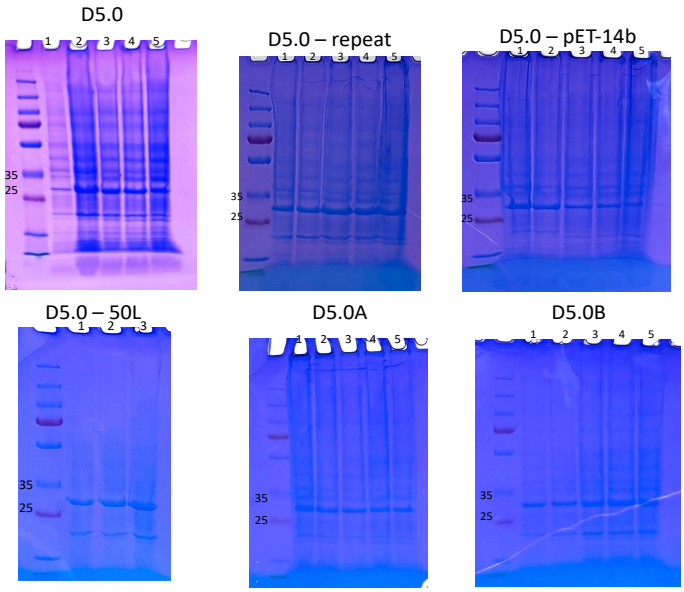


***Figure 2. Whole-cell SDS-PAGE showing expression of PCM protein TR8n8 for selected defined media runs with autoinduction. Labels are defined as in Figure T1. In each gel, lanes going from left to right reflect samples taken at later timepoints, and the rightmost lane is the culture at the time of harvest. The darkest band, occurring between the marker bands for 25 and 35 kd, is TR8n8 in each case.***

**Influence of sequence on yield:** As we prepared new PCM-protein sequences for thermal screening, we discovered variations in purified protein yield from batch to batch, and between different sequences. Figure 3a compares the wet biomass and purified protein yields from 18 independent 1-L flask-scale growths and DMSO/water purifications. Variability is expected between different sequences and also at every step of the process from growth to purification, and the number of tests per sequence is limited, so our conclusions must be tentative. However, two points can be made. First, certain sequences seem to be more amenable to higher-yield production than others. Of this set, those that were tested multiple times showed a correlation between biomass yield and purified protein yield, suggesting that attempts to increase biomass may successfully give more protein for these sequences (see TR31n8 and TR32n8). Other sequences behave less predictably, and do not show improvements in protein yield as biomass increases. The origins of the observed behavior are still unknown, but the relative propensity of coding sequences for recombination and relative toxicity of the protein products remain the most likely possibilities. This suggests that a more extensive scaled-down screening campaign should be applied to identify the PCM-protein sequences that are most amenable to high-yield production. Second, the results illustrate that whole-cell SDS-PAGE analysis is insufficient to predict the yield behavior of new sequences, and that an assay to quantify protein extracted and recovered from cells is needed to complete the proposed screening campaign. As a representative example, Figure 3b shows that TR31n8 appears more strongly expressed than TR32n8 in whole-cell SDS-PAGE, even though the later batch gave 60% more protein from the associated purification. Explanations range from trivial variability in solubility and staining of during SDS-PAGE to bona fide differences in extraction in and recovery efficiency during purification. Although the goal of the experiments in Figure 3 was to produce sufficient material of each sequence for thermal measurements, this effort gave the added benefit of guiding our upcoming efforts to discover PCM protein sequences that can be produced in higher yield.

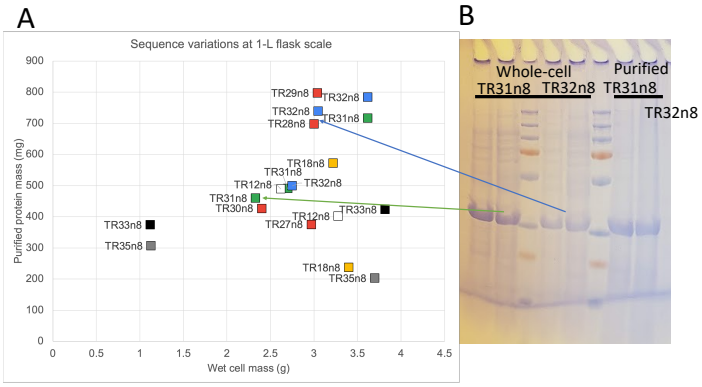


***Figure 3. A: Wet cell mass versus purified protein mass for a variety of PCM-protein sequences. In each case, the vector and strain were pET-14b and BL21(DE3), respectively. For each experiment, two 500 mL cultures were grown at flask scale and the biomass was pooled for a DMSO/water purification. Each PCM protein sequence was attempted either three times (TR31n8: green boxes; TR32n8: blue boxes), two times (TR12n8: white boxes; TR18n8: gold boxes; TR33n8: black boxes; TR35n8: grey boxes), or only once (TR27n8, TR28n8, TR29n8, TR30n8: red boxes). B: SDS-PAGE showing intrinsic variation in band intensity between different sequences. TR31n8 gives stronger bands than TR32n8 from whole cells, even though TR32n8 yielded 60% more purified protein in this experiment.***

**Improved purification processes:** The use of DMSO as an extraction solvent for the purification of PCM proteins offers numerous advantages, including: high extraction efficiency, one-step extraction without mechanical cell lysis, and high recovery efficiency with inexpensive antisolvents. However, we also anticipate several important challenges as the DMSO-based purification process is brought to the pilot and plant scales, such as the requirement of biomass drying, the safety and environmental concerns associated with the use of solvents above room temperature, and the energy and engineering costs associated with solvent recycling. To begin to address these challenges early in the development process, we screened a variety of alternative purification conditions, focusing on those with improved cost, safety, and environmental profiles. This effort produced several alternative options, the most promising of which was the discovery that TR8n8 PCM protein can be rapidly solubilized to concentration of least 40 mg/mL under aqueous alkaline conditions (25-75 mM NaOH) without organic solvent or other additives. The pH range under which the protein can be solubilized without hydrolysis is relatively narrow; based on the amino-acid composition of the protein, we hypothesize that solubilization is enabled by deprotonation of the phenolic groups of its tyrosine residues.

For effective purification, solubilized PCM protein must be recoverable in high yield with applications-performance maintained. To illustrate the utility of this aqueous alkaline solubilization for purification, we repurified a small (160 mg) batch of DMSO-purified TRT8n8 PCM protein by dissolving it in aqueous alkaline conditions and then dialyzing the solution against pure water using an inexpensive regenerated-cellulose membrane. As shown in Figure 4, the vast majority of the protein recovered as solid precipitate after dialysis against pure water (Pellets, A), while a small amount remains in the supernatant (Supernatants, A).

To investigate the possibility of complete recovery, we tested an ability of several ammonium sulfate concentrations to precipitate the remaining protein from solution. Figure 4 (B-E) shows that increasing ammonium sulfate concentrations precipitate increasing amounts of protein from the dialysis supernatant, with final concentrations of >= 4.5% sufficient to precipitate all protein detectable by SDS-PAGE.

To test the yield and behavior of the recovered protein, the original dialysis pellet material was further washed with water, frozen, and lyophilized. The measured mass was identical to the input quantity of 160 mg, suggesting minor errors in mass measurement or perhaps a true increase in sample mass due to derivatization to the sodium tyrosinate form of the protein. In any case, this result agrees with the SDS-PAGE that the vast majority of the protein could be recovered by simple dialysis. The resulting powder could be completely dissolved in HFIP and cast into a free-standing film; the resulting film exhibited the expected qualitative extensibility behavior when hydrated, strongly suggesting that the repurified, alkaline-treated material was equivalent to the original.

Notably, our aqueous alkaline conditions cause bacterial cell suspensions to clarify significantly, and similar conditions are frequently applied to extract plasmid DNA from bacterial cell pellets; these observations give optimism that a simple and scalable

procedure for aqueous alkaline extraction and purification of PCM protein can be developed.

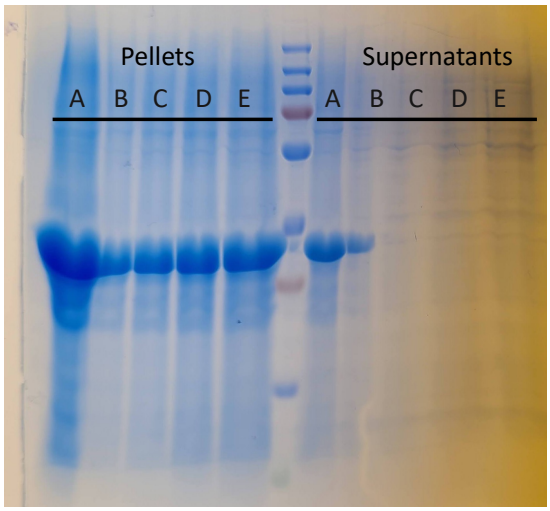


***Figure 4: SDS-PAGE showing the result of aqueous-alkaline repurification of PCM protein TR8n8. A: dialysis of aqueous-alkaline solution against pure water. B: dialysis supernatant, brought to 1% ammonium sulfate. C: dialysis supernatant, brought to 4.5% ammonium sulfate. D: dialysis supernatant, brought to 11.5% ammonium sulfate. E: dialysis supernatant, brought to 25% ammonium sulfate.***

## ii.b. Thermal conductivity and energy storage density of SRT PCM

**Thermal conductivity (4X switching with high thermal conductivities > 1 W $m^{-1}$ $K^{-1}$).** A major advance in the performance of the SRT PCM materials was the study of SRT purity on thermal conductivity switching. The processing steps used in creating the SRT PCMs led to changes in the thermal conductivity switching due to changes in composite purity. To understand the role of purification on the thermal conductivity switching of the protein films, we performed TDTR measurements on films with a variety of preparation methods; these measurements were performed in both ambient and 'hydrated' conditions (e.g., water is added to the protein and the thermal conductivity is measured). Ultimately, we found that when the preparation method was altered in any way, the thermal conductivity in the hydrated state was greatly inhibited; these data are shown in Fig. 5 for the TR8n8 protein produced by Tandem Repeat, where preparation method 'DMSO, $H_2O$' denotes our original purification method described in our prior work (*Nat. Nano.* **13,** 959). Following multiple repeat tests on two different TDTR systems that confirmed this critical finding, we determined the cause is a change, or lack thereof, protein folding during these purification methods. In other words, the structure of the SRT is greatly affected by the change in preparation. In particular, it appears that residual DMSO in these larger-scale purification methods inhibits the formation of crystalline beta-sheets in the SRT; these beta-sheets are critical towards the enhanced thermal conductivity of hydrated SRT.

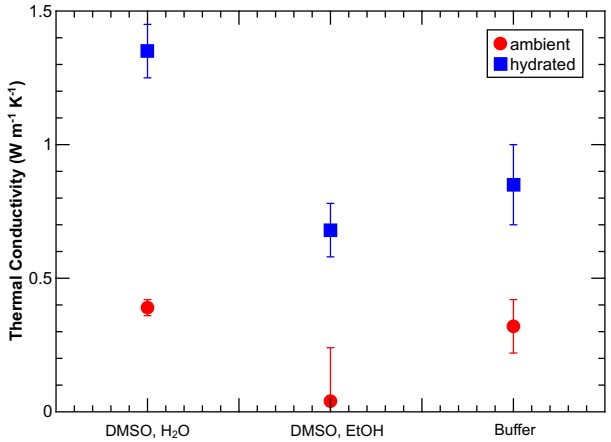


***Figure 5: Thermal conductivity switch of SRT thin films with varying purification techniques.***

In Fig. 6, we compare the protein sequence produced by Tandem Repeat (solid points) to the sequence used in our original work (*Nat. Nano.* **13,** 959), and note that there is a marginal increase in the hydrated thermal conductivity (and thus switching ratio) for identical repeat unit numbers. This indicates that the sequence can be further manipulated, in addition to chemical additives, to enhance the thermal conductivity of hydrated SRT. The increased purity and chemical additives on the proteins from Tandem Repeat produced here give rise to thermal conductivity switching that meets our goal of 4X thermal conductivity switching. Our range of thermal conductivity switching on this TR8n8 is $k_{max}/k_{min}$ ~ 3.0 – 4.1 based on the measured values and uncertainty. This approach of sequence design combined with chemical additives is showing promise to increase the thermal conductivity switching.

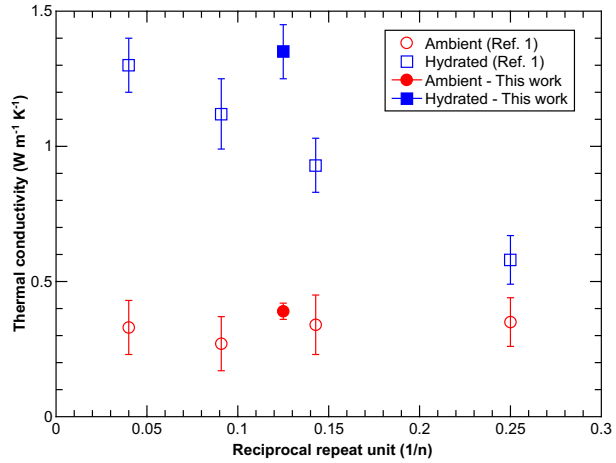


***Figure 6: Comparison of hydrated thermal conductivity values from our previous work (open symbols, Nat. Nano. 13, 959) and from SRT films synthesized with Tandem Repeat's protein sequence (closed symbols). The protein sequence developed by Tandem Repeat provides a marginal increase in the hydrated thermal conductivity, providing an additional route for manipulating thermal transport.***

We also studied the role of hydrating fluid composition on modulating the magnitude of the thermal conductivity switch of squid ring teeth (SRT) proteins. Since a protein's structure dictates its properties, such as thermal conductivity, varying the composition of

the hydrating solution will alter the structure of the protein's hydrated state, thus changing its thermal conductivity. Four different protein films and sequences were tested, shown below in Table 3. The four additives that were tested are glycine, trimethylamine N-oxide (TMAO), propylene glycol, and urea. All four additives are biological osmolytes. Glycine, and TMAO are stabilizing osmolytes, while urea is a destabilizing osmolyte.

***Table 3: SRT films tested for thermal conductivity switching under different working fluids. The Penn State sequence is the original sequence from the Nat. Nano. work. The F2 and F3 crystalline sequences are the original Penn State sequences, but two or three of the tyrosine residues have been substituted for phenylalanine. The identity of the Tandem crystalline sequence is unknown. The TR11n8 sequences are identical, but the DEH film was purified with DMSO, ethanol, and water, while the DH film was purified using only DMSO and water.***

| Sequence Name | Amorphous Sequence | Crystalline Sequence |
|---|---|---|
| TR11n8 (DEH) | Penn State – F3 | Penn State |
| TR11n8 (DH) | Penn State – F3 | Penn State |
| TR12n8 | Penn State | Penn State |
| TR17n8 | Penn State – F2 | Tandem |
| TR8n8 | Penn State | Tandem |

Glycine is not only an amino acid, but also a well-known osmolyte. In nature, osmolytes protect a protein's tertiary structure when they encounter potentially denaturing conditions. Glycine does this by depleting from the surface and reducing the oxygen-oxygen distances of the water molecules found in the inner most hydration sphere. The reduced oxygen-oxygen distance enhances the water structure and causes the protein to fold more tightly. The data for four of the films is shown below in Figure 7. Only TR11n8 (DH) is shown because the values for both films are within error of one another. As shown in Figure 6, the hydrated thermal conductivity for all films with a glycine hydrating solution are very similar to the pure water values. This shows the glycine has no preference for sequence when it comes to the thermal conductivity.

TMAO is a stabilizing osmolyte whose mechanism of action is highly debated in the literature. The osmolyte is found in many marine animals and is used to prevent protein denaturation under extreme hydrostatic pressure. The data for the four films hydrated using TMAO solutions of varying compositions is shown below in Figure 8. For the TR11n8, TR17n8, and TR8n8 films, there is an inverse trend between thermal conductivity and TMAO solution concentration. As the concentration increases, the thermal conductivity decreases. The decrease in thermal conductivity is reversed by removing the TMAO solutions and adding DI water to the films, shown as the blue circles in Figure 8.

The TR12n8 film has an interesting trend. The thermal conductivity increases up to the 2M solution and then begins to decrease. This increase is also seen after the TMAO is removed and DI water is added. Since the mechanism of action for TMAO is highly debated, we cannot explain exactly why this is occurring, but we are able to hypothesize. The TR12n8 film consists of the original SRT sequence reported in the original SRT work. Its amorphous segment contains long sections of hydrophilic residues, broken apart periodically by lysine residues. One theory for TMAO's mechanism of action is that it

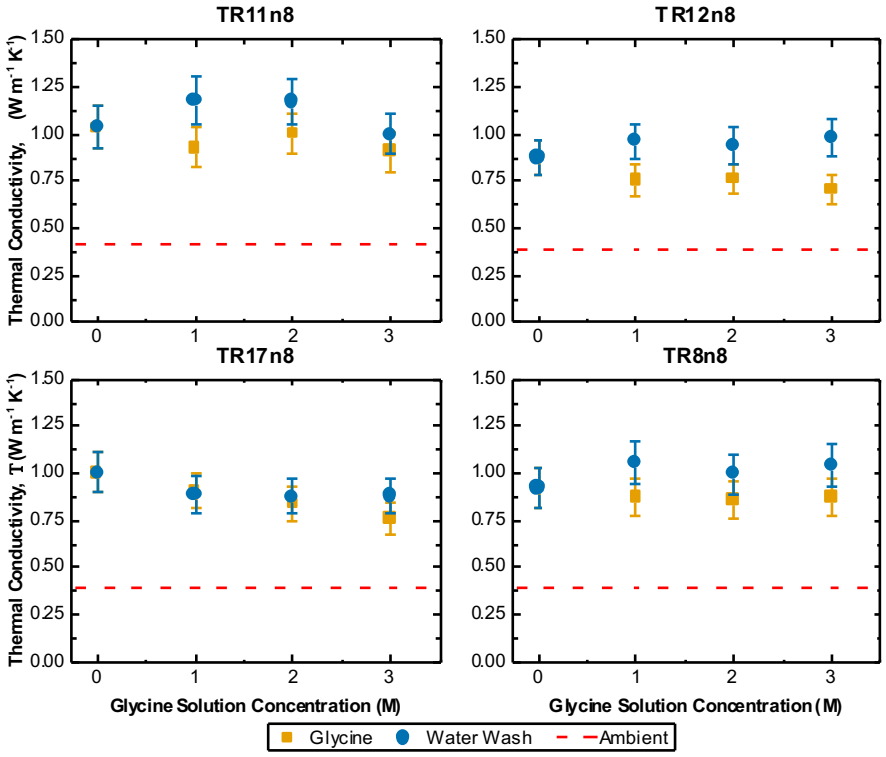


***Figure 7: The thermal conductivity trends for SRT films with glycine hydrating solutions.***

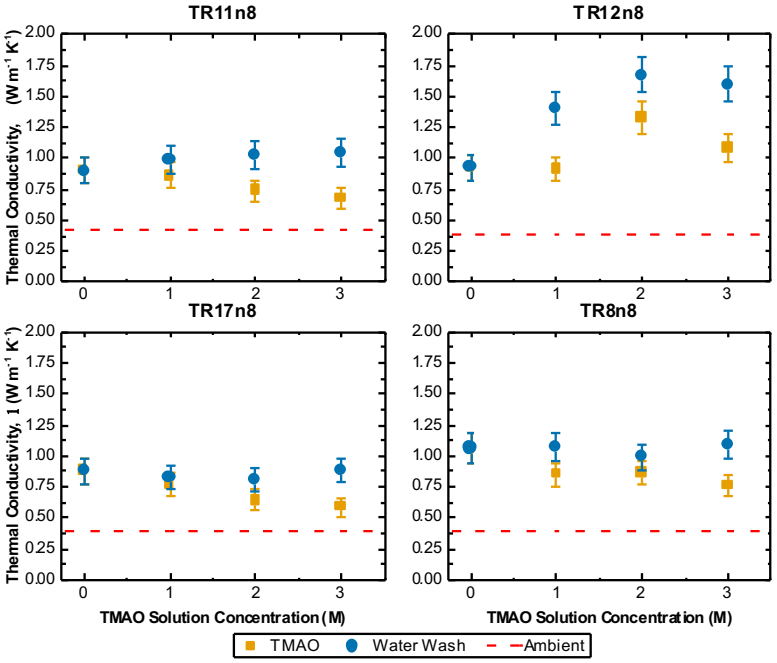


***Figure 8: The thermal conductivity trends for SRT thin films with TMAO hydrating solutions of varying concentrations.***

interacts with longer stretches of hydrophilic residues. By interacting with the hydrophobic residues in the amorphous region, the protein structure could be altered in some way to encourage the transport of phonons throughout the material. This does not occur in the other SRT films because they all contain modified sequences for either the amorphous or crystalline regions. The substitution of phenylalanine for tyrosine in the amorphous regions of the TR11n8 and TR17n8 films breaks up the stretches of hydrophilic residues. This would prevent the TMAO from interacting directly with the protein, thus reducing the thermal conductivity. Further experimentation will need to be done to probe the structural changes that may occur in the protein.

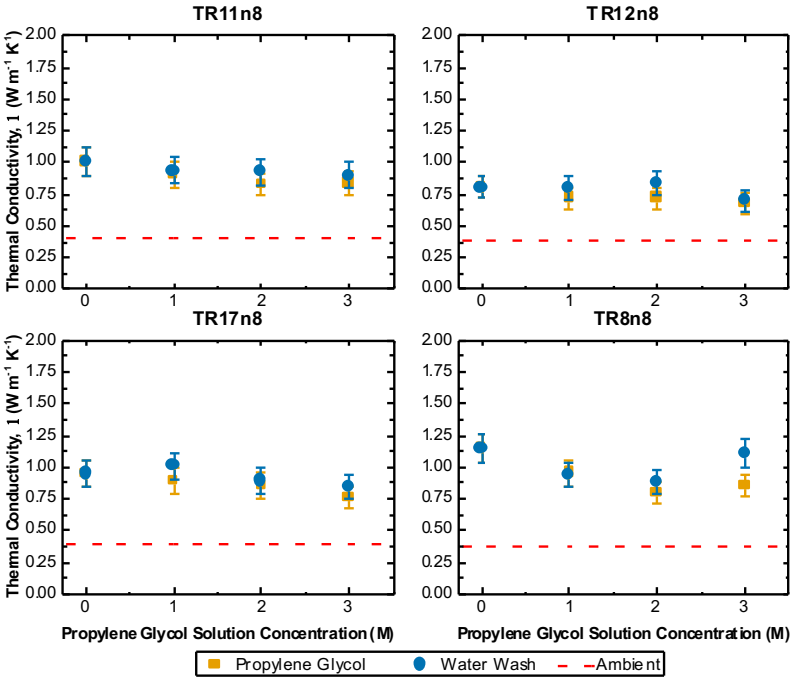


***Figure 9: The thermal conductivity trends for SRT thin films with propylene glycol hydrating solutions of varying concentrations.***

Propylene glycol was the third additive tested. It has a wide variety of applications, such as a precursor for the synthesis of polyesters and as an additive in pharmaceuticals. When it comes to its interactions with proteins, propylene glycol interacts in different ways. It was shown to disrupt hydrogen bonding and encourage helix formation within bovine serum albumin, while it did not have a denaturing effect on type I collagen. Since the Gly-Pro-Ala triplet in SRT has a similar mobility factor to the Gly-Pro-Hyp triplet in collagen, we can hypothesize that propylene glycol will not have a large effect on the thermal conductivity of SRT films. This hypothesis was confirmed, which is shown below in Figure 9. There are no differences between the SRT hydrated values when the films were hydrated with propylene glycol solutions or pure DI water. This indicates that protein sequence does not affect propylene glycol's mechanism of action.

The final additive tested was urea. Urea is an extremely well-known protein denaturing agent. It's mechanism of action is quite different from the other two osmolytes studied, as it directly interacts with the protein backbone and the amino acid sidechains. It was

previously shown to disrupt b-sheet formation and physical cross-linking within SRT protein strands. Figure 10 below shows the effect that urea hydrating solutions had on both TR11n8 films, as well as the TR17n8 and TR8n8 films. For this set of films, the urea has no effect on the thermal conductivity of the hydrated state. This is extremely surprising and needs to be investigated in future work. In contrast, the 1M urea solution destroyed the TR12n8 film. It occurred so quickly that we were unable to collect any data prior to denaturation. This could indicate that protein sequence does dictate urea's mechanism of action, but future work will be needed to determine exactly how.

In summary, hydrating solutions containing four separate additives were tested. Glycine and propylene glycol had similar interactions with the SRT films and did not depend on protein sequence. On the other hand, both urea and TMAO reacted differently based on the protein sequence. Future work should be focused on analyzing the exact structural changes each additive enacts on the SRT protein films.

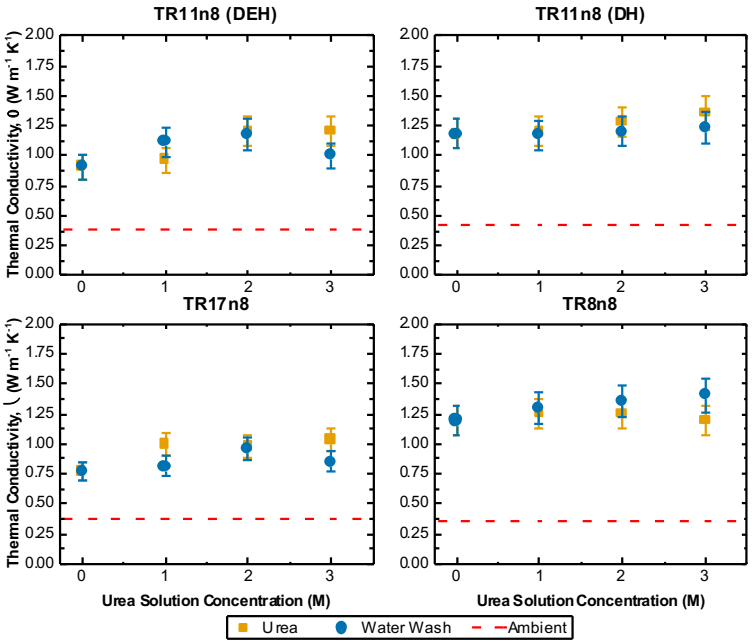


***Figure 10: The thermal conductivity trends for SRT thin films with urea hydrating solutions of varying concentrations.***

**Energy Storage Density (> 30 kWh m$^{-3}$).** Our initial assessment of the increased energy storage capacity of the hydrated SRT by considering the specific heat of the fraction of water that is stored in the sample and the ratio of crystalline and amorphous domain sizes in the sample. In these initial TR8n8 samples, we approximate the water content based on prior thermogravimetric measurements to be ~40%, resulting in glass transition temperature of the hydrated proteins of -39 degrees Celsius. The glass transition temperature shift yields an energy storage density of 16 kWh m$^{-3}$. In our system level design, by slightly increasing the temperature of the plasticizing fluid relative to ambient we can also increase energy storage density by sensible heat gain. For example, by increasing the temperature to 39 degrees Celsius, the energy storage density of the hydrated TR8n8 proteins is 37 kWh m$^{-3}$. This initial measurement of energy storage

density is based on the protein engineering of amorphous and crystalline regions to maximize water absorption in addition to system level concepts to store the absorbed thermal energy at a higher temperature relative to ambient. This finding additionally provides a clear path to maximize energy storage density even further by protein engineering to drive down the hydrated SRT PCM's glass transition temperature relative to that of the dry state, and designing the energy storage and heat exchange system to operate by storing the recovered thermal energy in the hydrated SRT PCM above ambient temperature.

A major technological advance towards energy storage density was in the application of a new metrology to measure the thermal conductivity of PCMs. When the SRT materials are produced at scale, we can measure the energy storage properties with more traditionally used techniques, such as differential scanning calorimetry. However, in these thin films, as we are evaluating the optimal genetic sequence, purity and additives needed to maximizing thermal conductivity switching and energy storage, we can not use these traditionally used measurement tools. Thus, applied a new thermal conductivity measurement technique to these SRT PCM films – steady state thermoreflectance (SSTR – *Rev. Sci. Instrum*. **90**, 024905) – a pump-probe technique that relies on measuring the steady state thermal response of materials, to measure the thermal conductivity of PCMs directly without having knowledge of heat capacity. This, in tandem with TDTR to measure the thermal effusivity of PCMs, allows for independent measurement of both thermal conductivity and heat capacity, and during phase transitions/shifts in glass transition temperatures of our SRT PCMs, allows for energy storage density measurements. We have used SSTR to benchmark the thermal conductivity of standard PCMs in tandem with TDTR to measure their thermal effusivities. Between these two techniques, we can determine the thermal conductivity and heat capacity of the PCMs.

We evaluated the thermal conductivity of standard, commercially available PCMs using SSTR as a calibration of this technique. We started with a commercial PCM from PureTemp, PureTemp37. To conduct SSTR measurements, we first deposited ~80 nm of Al on a transparent calibrated pure silica glass slide. We then melted the PureTemp on the Al and allowed the PCM to solidify on the Al surface, and then conducted SSTR measurements through the glass, monitoring the reflectivity at the glass/Al interface. In a SSTR measurement, the thermoreflectance of the Al surface is monitored as a function of pump-power. The thermoreflectance is related to temperature and the pump-power is related to heat flux, and thus, the response is Fourier-like and related to the thermal conductivity of the adjacent materials. Thus, the change in SSTR data from the glass/Al/air sample to the glass/Al/PureTemp37 sample is an indicator of the thermal conductivity of the PureTemp37. These data are shown in Fig. 11. The "Air" sample is used as a measurement control, and the SSTR signal on this sample is indicative of a heated Al film discharging its energy into the glass with the Al/air side being relatively insulated. Thus, the thermal conductivity of the measurement volume of air is calibrated to $k$ = 0.03 W $m^{-1}$ $K^{-1}$ as labeled in the plot. When the PCM is in contact with the Al film thermometer, the shift in SSTR signal indicates that energy from the laser heated Al is flowing into the PCM, and thus our SSTR measurement is sensitive to the thermal conductivity of the PCM. With the steady state solution to the cylindrically symmetric heat

equation solved for multilayers, we determine that the thermal conductivity of the PureTemp37 is 0.21 W $m^{-1}$ $K^{-1}$, in good agreement with the manufacturer specs, thus providing an initial benchmark of SSTR for measuring the thermal conductivity of PCMs. SSTR and TDTR measurements will be used to measure energy storage density of the SRT PCMs (TR8n8) during the water absorption measurements discussed above.

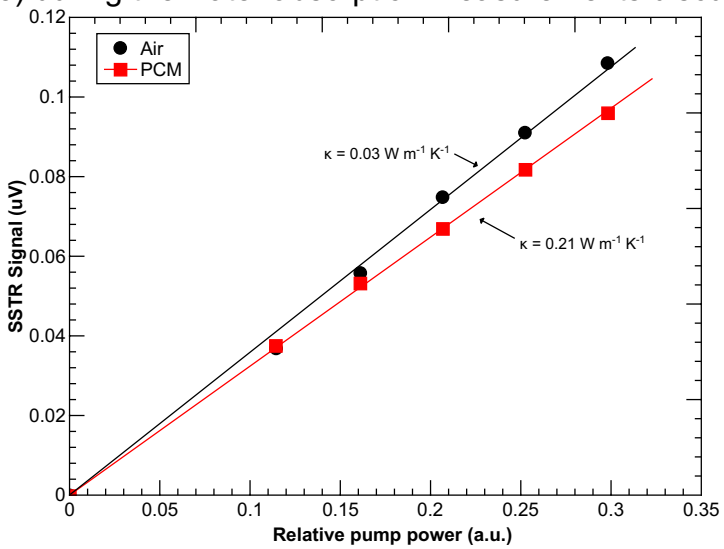


***Figure 11: SSTR data taken on an aluminum coated glass slide (black circles, "Air") and an Al coated glass slide with a commercial PCM (PureTemp37) in contact with the Al (red squares, "PCM"). The "Air" sample is used as a measurement control, and the SSTR signal on this sample is indicative of a heated Al film discharging its energy into the glass with the Al/air side being relatively insulated. Thus, the thermal conductivity of the measurement volume of air is calibrated to k = 0.03 W $m^{-1}$ $K^{-1}$ as labeled in the plot. When the PCM is in contact with the Al film thermometer, the shift in SSTR signal indicates that energy from the laser heated Al is flowing into the PCM, and thus our SSTR measurement is sensitive to the thermal conductivity of the PCM. With the steady state solution to the cylindrically symmetric heat equation solved for multilayers, we determine that the thermal conductivity of the PureTemp37 is 0.21 W $m^{-1}$ $K^{-1}$, in good agreement with spec, thus providing an initial benchmark of SSTR for measuring the thermal conductivity of PCMs.***

Given this SSTR approach, we have developed the ability to measure heat capacity independently of other thermal properties such as thermal conductivity or thermal boundary resistance (TBR). Steady-State Thermoreflectance (SSTR) is insensitive to heat capacity if the modulation is kept within the steady state regime (modulation is slow enough such that the temperature rise under a single modulation event brings the heated volume to a temporally constant temperature), but is able to measure a single other unknown (e.g., thermal conductivity or thermal boundary resistance). Time Domain Thermoreflectance (TDTR) is typically sensitive to the thermal effusivity however (i.e., equally sensitive to heat capacity and thermal conductivity). As mentioned above, combined, this means that if a thermal conductivity is measured via SSTR, the thermal effusivity from TDTR can be used to find the heat capacity. Similarly, SSTR outside of the steady state regime may still be sensitive to heat capacity, meaning SSTR can be done at multiple frequencies and/or spot sizes to extract both parameters. This is visualized below via contour plots (Fig. 12), where SSTR at 1 kHz is insensitive to the heat capacity of sapphire (vertical contours: any value for heat capacity yields an acceptable fit to data if the appropriate thermal conductivity is used in the model), while SSTR at 10MHz is roughly equally sensitive (contours with a slope of approximately -1: thermal conductivity

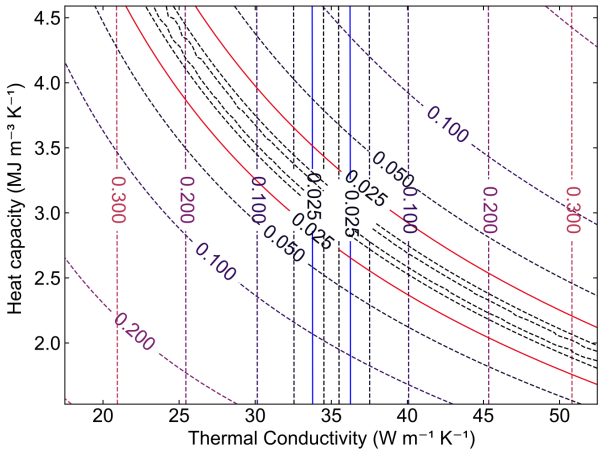


***Figure 12. Contour plots show the quality of fit (contours) as a function of each thermal parameter (x and y axes, thermal conductivity and heat capacity). Combinations which yield acceptable fits (e.g. a residual of model to data below 2.5%) are identified with a solid line. SSTR at neither frequency independently can resolve both thermal conductivity and heat capacity independently, however, the range of values which satisfy both experiments is limited.***

or heat capacity can be increased by the same amount i n the model to achieve an identical fit to data). While neither measurement is independently able to fit for both parameters, when combined, the combinations of parameters which satisfy both experiments are limited.

In order to measure enthalpy of melting, a similar cyclic heating is performed as SSTR, however the laser power used is significantly higher (capable of producing temperature rises of upwards of 100 K, as compared to the merely perturbative heating applied under traditional SSTR or TDTR). Each cyclic heating event also must be allowed to fully melt and resolidify the measured region of the sample, meaning lower modulation rates are also used. Finally, a periodic waveform analyzer (PWA) is used to capture the temperature rise, plateau due to melting, peak temperature, cooling, and plateau(s) due to resolidification and/or crystallization. This process that we can now monitor with a thermoreflectance signal for a thin film is shown in Fig. 13.

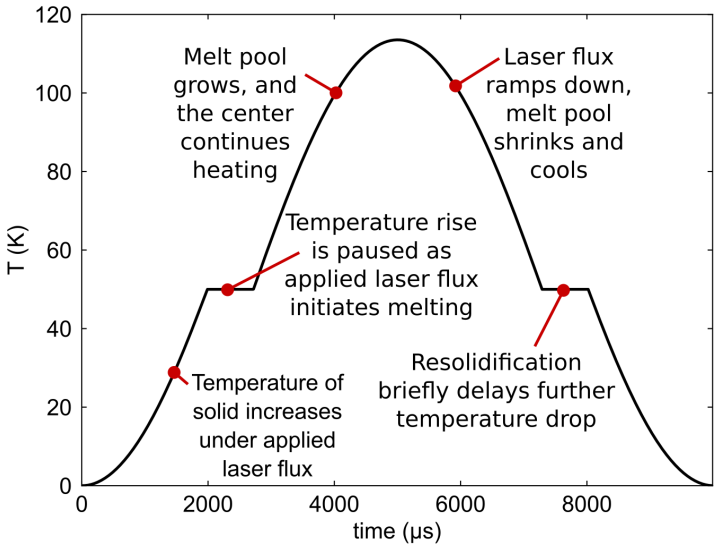


***Figure 13. The fundamental principle of operation is demonstrated via a simplified schematic for the expected temperature trend resulting from sinusoidal laser heating and laser-induced melting. Prior to melting, laser flux serves to increase the temperature of the sample up to the melting temperature. Once the melting temperature is reached however, laser flux contributes to melting rather than a temperature increase, which yields a time lag associated with melt pool formation. As a first approximation, the size of the plateau is indicative of the enthalpy of melting.***

Our SSTR system consists of a 100 mW Obis LX laser at 637 nm (pump) which is digitally modulated. The beam is directed through a Mitutoyo 20x magnification microscope objective lens to focus it onto the sample surface. A portion of the pump beam is also directed to a photodetector, which serves as a reference to monitor the pump's power. A second 70 mW Obis LX laser at 785 nm is also used as a probe; similarly directed through the same objective lens and reflected off the sample. Both pump and probe paths are fiberized until they reach the microscope objective, requiring minimal alignment, and allowing for great control over the beam profiles and sizes upon reaching the sample. For melting, we use a 15 W Spectra Physics Milennia eV laser at 532 nm, which is chopped at frequencies ranging from 100 Hz to 600 Hz. This laser is not fiberized, but is collimated with the fiberized pump and probe lasers immediately prior to entering the microscope objective. A lens pair is used upstream to adjust the beam size entering the microscope objective, which allows for a limited degree of independent control of the heater beam's focused spot size. We use a Zurich Instruments UHF Lock-in amplifier to monitor the probe response, locking in to the same frequency at which either pump or 15 W heater beam is modulated. For SSTR, the AC component of the probe response is monitored, as any changes in reflectivity of the sample occurring at this frequency can be considered to be solely due to modulated heating. For enthalpy measurements, the waveform of the probe response is monitored, allowing capture of the periodic temperature rise / melting curve. We demonstrate this approach on a sample of parrain and bulk Ga, as shown in Fig. 14.

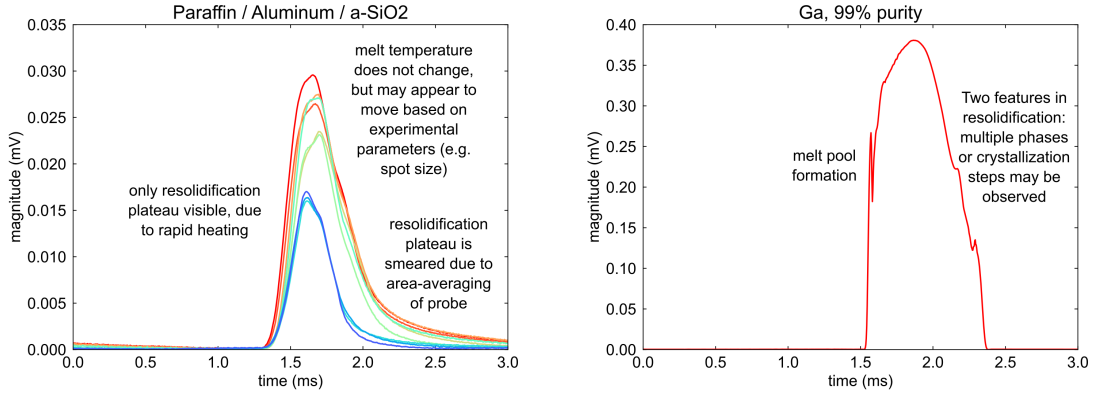


**Figure 14. Left: Paraffin wax is melted on an aluminum-coated glass slide, where the aluminum serves as the transducer for the thermoreflectance experiments. Melt signatures can be seen, however they deviate substantially from the idealized model pictured above. If the sample is heated too rapidly, the melt plateau may not be captured. similarly, since the probe is effectively taking a weighted average over its area on the sample, and since the aluminum itself may continue to heat as the PCM melts, the plateau may be smeared. Right: Bare Gallium metal is pumped/probed directly. This negates the heating effect of the aluminum, but may result in other complications to the data. For example, if the surface topology of the solid vs molten sample differs, or if the thermoreflectance coefficient (dReflectivity/dTemperature) differs, this will greatly complicate analysis.**

For measurements on hydrated squid protein polymer, deposition of aluminum directly on polymer would not be possible. Instead, a glass slide is coated in aluminum, and the polymer is affixed to a portion of the aluminum side of the slide (in a similar geometry to the parrafin control in Fig. 14). This allows measurement and laser-applied heating

through the glass, and the regions without protein attached can serve as the reference for the magnitude-based thermoreflectance measurements. The reflectivity of heating beam off the sample is found by measuring the unfocused incident and reflected power. This value, in combination with the thermal properties of the sample stack, is critical to predicting the temperature rise under exposure to the heating beam; a step not ordinarily required when an electrical resistive heating stage is used.

The low frequency (1 kHz) and high frequency (10 MHz) reference sample data is analyzed first. Note that while optics and material absorption and thermoreflectance coefficients are unlikely to be frequency-dependent, other components may be, such as the efficiency of the digital modulation of the laser or the detection capabilities of the photodetector(s). Next, the low frequency data (insensitive to heat capacity) is used to fit for the thermal conductivity. once the thermal conductivity is known, the high frequency data (approximately equally sensitive to thermal conductivity and heat capacity) can be used to fit for heat capacity. This results in the following values for heat capacity at room temperature and at 60 K above room temperature, shown in Table 4.

**Table 4: Measure heat capacities in dry and hydrated states, including when applying temperature change from the laser heat in our nano-DSC pump-probe laser system**

| Sample | $C$ (MJ $m^{-1}$ $K^{-1}$) |
|---|---|
| Dry SRT, room temperature | 1.70 |
| Hydrated SRT, room temperature | 3.08 |
| Hydrated SRT, $\Delta T$ = 60 K | 3.52 |

From this, we determine the energy density of the hydrated SRT at 60 K relative to that at room temperature, and relative to that of the dry states, shown in Table 5. For comparison, we show the energy density from sensible heat storage of water over the same temperature range.

**Table 5: Energy storage densities of hydrated SRT**

| Sample | $E$ (kW hr $m^{-3}$) |
|---|---|
| Hydrated SRT at DT = 60 K relative to dry SRT at room temperature | 112 +/- 13 |
| Hydrated SRT at room temperature relative to hydrated SRT at room temperature* | 28 +/- 5 |
| Water (reference) | 70 |

**This is akin to a "latent heat". Note, SRTs do not exhibit a typical first order phase transition with a latent heat effect that we would observe in a solid->liquid transition. Since the glass transition in SRT shifts downward with hydration, the difference in sensible heats from dry to hydrated at any given temperature relative to the glass transition temperature ($T_{glass,hydrated}$ = 219 K) gives the energy storage density at room temperature that would be equivalent to a "latent heat". Due to the temperature dependence of the heat capacity and the increase in the difference in dry and hydrated energy storage with temperature, this energy storage density in the SRT is temperature dependent.*

As clearly demonstrated in Table 5, the hydrated SRT exhibits additional energy storage capacity beyond the water alone which we attributed to our hypothesis of the plasticization of the SRT due to the reduction in the glass transition temperature. Thus, just from

sensible heat storage alone over a modest $\Delta T$, we have achieved the End of Project Milestone for Task 2.1.2 for the energy storage density in hydrated SRT within our experimental uncertainty. Further, when comparing the energy storage density of the SRT relative to a dry SRT at room temperature, the energy storage density can reach out stretch target, offering a unique energy storage mechanism that can inform the design of energy storage systems for complete hydration/dehydration of the SRT protein.

**Durability (Repeatability of >75% over 100 cycles).** Our durability evaluation of the SRT's thermal conductivity and energy storage metrics has been focused on the new SSTR technique capable of measuring the pure thermal conductivity of PCMs without convolution of thermal storage effects. While this allowed for high-fidelity measurements of the energy storage density and thermal conductivity of SRT materials, we were ultimately relying on two separate techniques to obtain these values (TDTR and SSTR, respectively). To overcome this, we have continued development of a new method, PWA-SSTR, to simultaneously measure the thermal conductivity and storage capacity of thin films without a priori knowledge of the material's thermophysical properties.

This experimental method is similar to SSTR, in that a periodically-modulated laser source induces a steady-state temperature rise on the surface of the sample of interest, while a second laser probe acts as a thermometer by monitoring the temperature-dependent reflectivity of the surface. However, in contrast to SSTR where we utilize standard lock-in amplification techniques for determining a time-averaged reflectivity value (i.e., standard SSTR provides a single value of reflectance for each pump power investigated), we implement an electronic periodic waveform analyzer (PWA) to monitor the *time-dependent* change in reflectivity of the sample surface during modulated heating. While the peak magnitude of this reflectance is identical to the data obtained in SSTR (i.e., the peak signal magnitude is indicative of solely the sample thermal conductivity, $k$), the temporal component is proportional to the thermal diffusivity ($C_V/k$) of the material system. This technique fills a critical gap in experimental metrologies, as it is analogous to a laser-based, micro-scale differential scanning calorimeter, with the added capability of extracting thermal conductivity.

Previously, we demonstrated this technique on 'standard' PCM materials (c.f., Fig. 11), such as Paraffin wax. We have thus implemented this novel experimental metrology to the SRT materials of interest. An example of these data for a TR8n8 film is shown in Fig. 15, with key aspects of the analysis labeled. In a single scan, we obtain two key parameters: the difference in minimum and maximum thermoreflectance signals (indicative of *only* the material's thermal conductivity), and the time constant associated with the transient evolution between this maximum and minimum (indicative of the material's thermal diffusivity, $Cv/k$). With this in mind, Fig. 15 displays PWA-SSTR data for TR8n8 in both ambient and hydrated environments. Despite the large offset between data, we note that the curvatures may appear relatively similar – the large similarity between data is due to the thermophysical properties of the substrate and thermo-optical transducer used for this metrology technique. However, using a multilayered thermal model, we can reliably extract the difference in thermophysical properties between the two states.

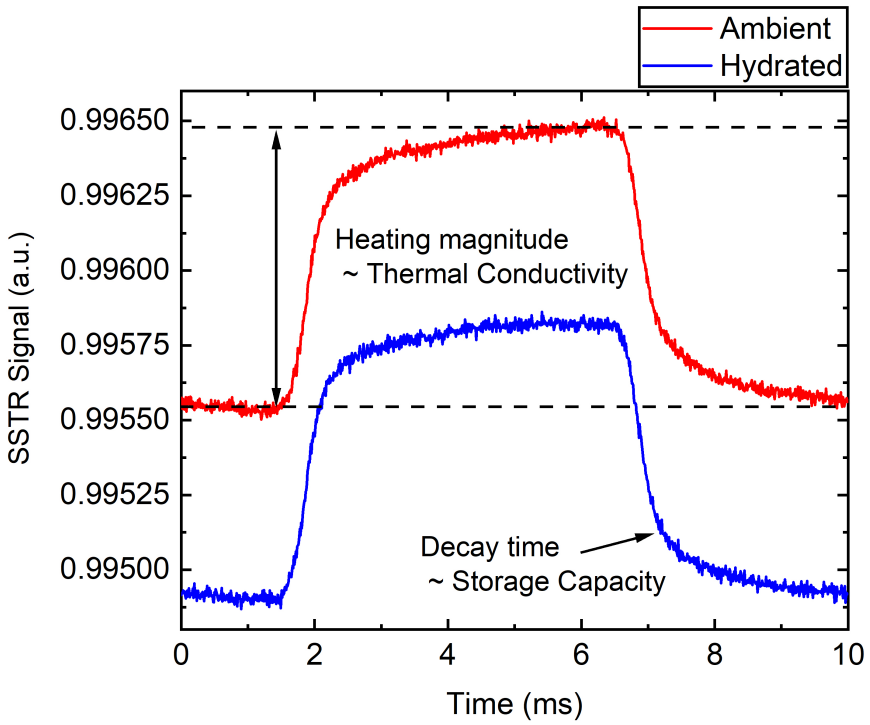


***Figure 15: Thermoreflectance magnitude (y-axis) as a function of time during modulated laser heating of SRT materials in both ambient (red line) and hydrated (blue line) conditions. Each curve represents a single scan with an acquisition time of < 5 seconds. This PWA-SSTR technique relies on measuring the relative heating magnitude (e.g., min-to-max thermoreflectance magnitude during heating/cooling) as well as the time constant associated with the transient evolution between this minimum/maximum states; these variables are linearly proportional to the thermal conductivity and thermal storage capacity of the material, respectively.***

With this new PWA-SSTR method, we have not only repeated the durability of the SRT material's thermal conductivity switching over 100 cycles with a second technique, but simultaneously measured the durability of the SRT material's *storage capacity* switching over 100 cycles. These data are shown in Fig. 16. On the left, the change in thermoreflectance magnitude, proportional to the SRT material's thermal conductivity, is shown over 120 hydration cycles, while on the right, the relative heating time in PWA-SSTR is plotted over these same cycles. Note: Each value is obtained from a *single measurement* – greatly accelerating the testing of thermal storage materials of interest.

We note two salient features from these data. First, the thermal conductivity shows the same high durability repeatability as demonstrated via TDTR measurements; a factor of 4x switching is observed consistently over these cycles. The few outliers are likely due to small differences in time scales before obtaining the scans; as this PWA-SSTR approach relies on relatively thick (> 50 um) SRT films, the time scale associated with hydration can be slightly variable based on variations in local film thickness (e.g., a 55 μm film may require thirty seconds for full thermal switching, while a 50 μm thick film may only require twenty-five seconds to achieve its maximum switching factor). The second feature is that the storage capacity shows similar long-term durability over the same 120 cycles. However, there is an increase in the number of 'outliers' when compared to the

repeatability of the thermal conductivity switching factors. While this observation requires further attention moving forward, through rigorous uncertainty analysis, we believe these apparent-deviations would be less prominent when sources of error in the analysis are fully accounted for.

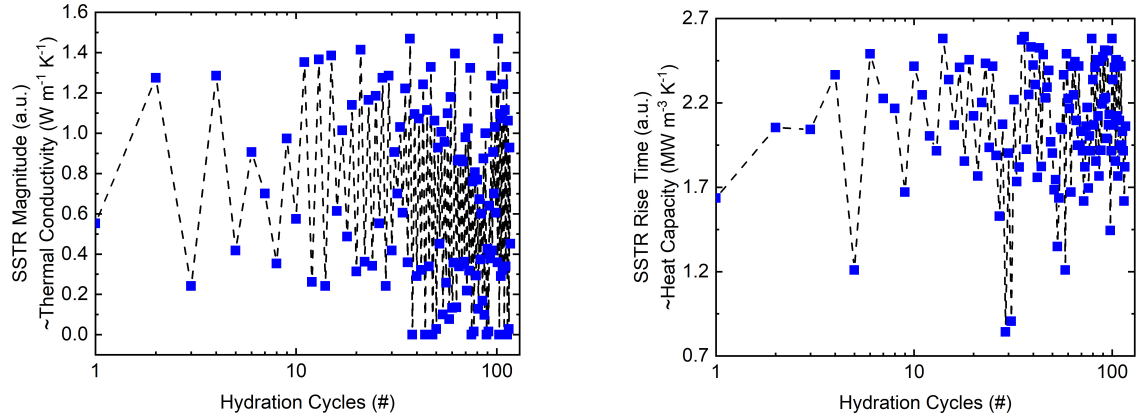


***Figure 16: Left: The heating magnitude of the PWA-SSTR signal over 120 switching cycles. This magnitude is directly proportional to the thermal conductivity of the SRT material; the data is scaled for representation, but displays minimal degradation of a factor of four switching in thermal conductivity. Right: Exponential time constant of the transient evolution during heating/cooling cycles during PWA-SSTR. Despite larger error than the magnitude component, reproducibility over 120 cycles remains evident.***

## ii.c. Techno-economic analysis

We have used thermodynamic and cost analyses to evaluate different system concepts. To begin this process, we identified three different system concepts. The first is an air conditioning evaporator air handler unit, filled with the PCM. This allows the PCM to directly exchange heat with the refrigerant and with the process air that flows through the air handler.

The second system concept that was identified was an evaporative cooler concept. In this system, the system would be hydrated with liquid water, which, due to the glass transition, would cool air flowing over the PCM. Then, dry air could be flowed over the PCM, which would release heat (due to the reversal of the prior glass transition process), but it would also absorb the latent heat of water as the water evaporates. Thus, the dehydration would still provide a net cooling (as the latent heat of water is very high). We are currently evaluating the merit of this system: an evaporative cooler that provides some of its cooling during the initial charging with water and the remainder of its cooling as it exchanges water with dry air. This is opposed to a conventional evaporative cooler, where all cooling is provided in the mass exchange step.

The third system concept that was identified was a desiccant system, in which the SRT PCM would be used as a desiccant dehumidifier. One of the benefits of the SRT PCM

are the increase in thermal conductivity upon hydration, which would allow the PCM to more easily reject heat to the ambient.

After identifying the different system concepts, we rank-ordered them based on the potential merit of the different designs, in order to determine which concept should be analyzed first. We decided that “heat exchanger” air conditioning air handler concept holds the most merit, so we have begun analyzing it first. This is pictured in Fig. 17.

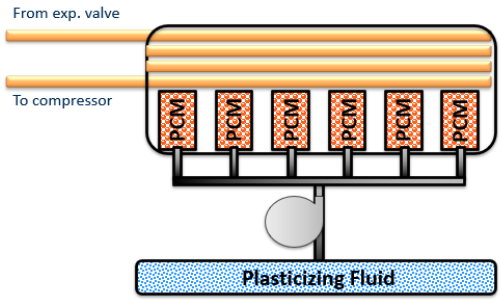


***Figure 17. A proposed air conditioning evaporator filled with SRT PCM. The PCM is isolated from exchanging mass with the environment, but it is in good thermal contact with the air and refrigerant that flow through the air handler. Plasticizer would be pumped in and out of the PCM to bring about thermal switching, which could be done rapidly, during the transient operation of the air conditioning system. This would allow the PCM to handle a portion of the cooling load during times when the air conditioning COP is low.***

In this system, the PCM must be isolated from the air, such that the plasticization of the PCM can be actuated, but the PCM must remain in good thermal contact with the refrigerant and the air. Upon plasticization, the PCM absorbs heat from its surroundings, undergoing a 100 kWh/m$^3$ phase transition. This is the discharging step. Then, to recharge the PCM, the plasticizer must be removed, which would release the heat of phase transition. In our design, the PCM could be rapidly actuated to handle a portion of the air conditioning load during transient operation throughout the day. While a typical system is charged once (at night) and discharged once (often during peak hours), our system could potentially be charged and discharged each time the air conditioner turns on. Assuming our goal of one cubic meter of PCM providing 100 kWh of energy storage for each time that it is cycled, using this stored energy for more than one cycle per day effectively increases the energy storage density of the material. This cuts down on the amount of PCM required, which reduces both PCM and system costs, as a more compact air handler unit could be utilized following the reduction in PCM volume. The goal of the system is to allow the PCM to handle a portion of the air conditioning load when the COP of the air conditioner falls during transient operation, due to fluctuating ambient outside conditions. After the COP goes back up, the plasticizer would be removed, and the released heat would be removed by the refrigerant.

After rank ordering of these three system designs, the concept that we determined to have the most merit is a “no insulation” room temperature storage concept, which is highlighted in Fig. 18. The second system concept is very similar to the first, except that the sensible charging step would be performed at night, instead of immediately before the discharge step. This maximizes the energy savings of the system and is useful if the “latent” storage capacity is comparable to the sensible capacity. The energy savings benefit of the second system concept comes at the cost of requiring insulation. The third system concept that was designed was a “multiple daily use” concept, in which the PCM would discharge alongside the air conditioning (thus reducing the required cooling power of the air conditioning) every time the air conditioning turns on. Then, when the building

reaches the desired temperature, the PCM would be recharged. This would allow the cooling system to spread out its cooling load over a longer period of time, which improves the cycle COP. However, preliminary results show that this concept provides less energy and cost savings than the other two concepts, so we have ranked this concept as the least viable. We have completed finite-time thermodynamics and simple payback analyses of the first system concept.

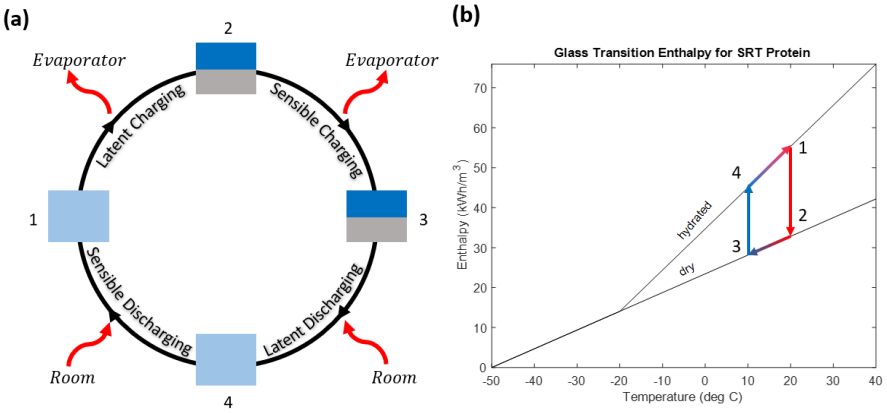


***Figure 18. Illustration of the first system concept. (a) shows the operation of the storage cycle, while (b) shows the operation plotted on an enthalpy vs temperature graph. In this system, the PCM is charged at night by removing the plasticizing fluid. This process releases heat, which must be removed by the evaporator. This can be performed at room temperature. The sensible charging step is performed immediately before peak hours and uses the evaporator to lower the temperature of the PCM. In the next step, latent discharging, the PCM is hydrated isothermally, which allows it to absorb heat from the room. After hydration, the sensible discharging step is performed, in which the PCM absorbs heat from the room while the temperature of the PCM approaches room temperature.***

To analyze the first system concept, we derived the governing equations for the storage system used in conjunction with an endoreversible vapor compression cooling system. The electricity required to charge the PCM at night ($W_c$) is given in Eq. 1, while the electricity saved by avoiding vapor compression work during PCM discharge ($W_d$) is given in Eq. 2. The *K* terms are conductances (i.e. the heat exchanger UA values), where $K_{EL}$ is the conductance between the evaporator and the building air, $K_{SL}$ is the conductance between the PCM and the building air, $K_{ES}$ is the conductance between the evaporator and the PCM, and $K_C$ is the conductance between the condenser and the ambient outside air. The evaporator temperature is $T_E$, and the hydrated glass transition temperature is $T_{g,w}$. The temperature of the ambient outside air at night (during charging) is $T_{\infty,c}$, while the temperature of the ambient outside air during peak hours (discharging) is $T_{\infty,d}$. The difference between $T_{\infty,c}$ and $T_{\infty,d}$ is the primary driver for energy savings. The amount of time that the PCM must provide cooling during discharging is $t_d$.

$$W_c = \frac{K_{EL} t_d (T_{room} - T_E)}{T_E} \left( \frac{T_{room} - T_{g,w}}{T_{room} - (K_{EL}/K_{SL})(T_{room} - T_E) - T_{g,w}} \right) \left( \frac{K_C T_{\infty,c}}{K_C - K_{ES}(T_{room} - T_E)/T_E} - T_E \right) \quad (1)$$

$$W_d = \frac{K_{EL} t_d (T_{room} - T_E)}{T_E} \left( \frac{K_C T_{\infty,d}}{K_C - K_{EL}(T_{room} - T_E)/T_E} - T_E \right) \quad (2)$$

The daily electricity savings are then $W_{saved} = W_d - W_c$, while the cost savings are $C_{saved} = W_d * C_d - W_c * C_c$, where $C_c$ is the cost of electricity during charging (at night) and $C_d$ is the cost of electricity during discharging (peak hours). Using NOAA data for daily air temperature in Arizona, as well as electricity pricing from Arizona Public Service, we performed the energy and cost savings analysis for every day of the year and summed the results to find the total year electricity and cost savings. The results from the cost savings analysis can be found in Fig. 19. We found that the hydrated glass transition temperature ($T_{g,w}$) can significantly affect the storage capacity (and thus the energy and cost savings) of the thermal storage system. By lowering $T_{g,w}$ in the hydrated SRT PCM from -20 degrees Celsius (the current value for the material) to -50 degrees Celsius (a feasible value that could be reached by improving the material/plasticizer), the energy savings increase by over 20%.

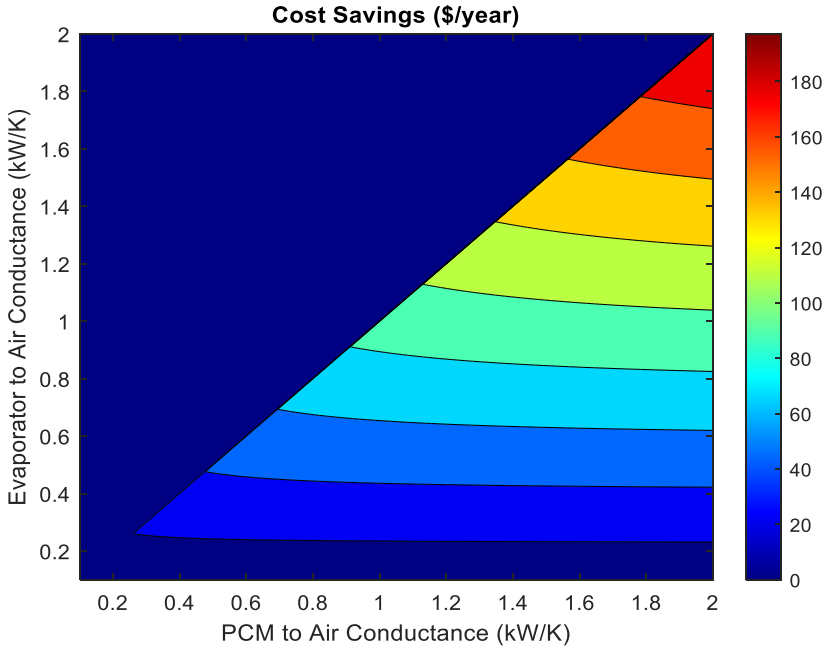


***Figure 19. Contour plot of yearly cost savings as a function of the conductance between the PCM and building air (x-axis) and the conductance between the evaporator and the building air that is being avoided by using the PCM (y-axis). For this analysis, sub-hourly outside temperature data from Yuma, AZ was used, along with an off-peak electricity price of $0.10/kWh and an on-peak electricity price of $0.23/kWh.***

The equations used for the thermodynamic analysis were derived using endoreversible or “finite time” thermodynamics, which does not account for internal irreversibilities within the system (exergy destruction in the expansion valve and compressor of the vapor compression cooling system). We have derived the equations for the more complex, internally irreversible analysis and implemented them into a Python script. However, this analysis takes far longer to run, so we utilized the endoreversible analysis to obtain preliminary results. When calculating the system payback time, we currently use a flat value of $15/kWh (the project target), independent of other system parameters, like the PCM to air conductance. In reality, these system parameters will affect the system cost, meaning that the system cost is not only tied to storage capacity but also to cooling power.

Presently, we have conducted the energy and cost savings analyses for a single location (Yuma, AZ), using the temperature and electricity pricing data for that location. We could then create a map which shows the energy and cost savings potential of the PCM system for each region within the US.

Additionally, we have generated a method for analyzing and evaluating the thermal system component. This has involved finding analytical solutions for the temperature distributions of the materials within the heat exchanger component. Once the temperature distribution solutions are found analytically, they can be converted to a MATLAB script that can numerically solve for the temperature distribution in the entire system. This temperature distribution can then be utilized in the first and second law analyses to evaluate the effectiveness of the system for various input parameters. The figure below shows the starting point for the analytical solutions, a single aluminum fin, coated on both sides with SRT polymer.

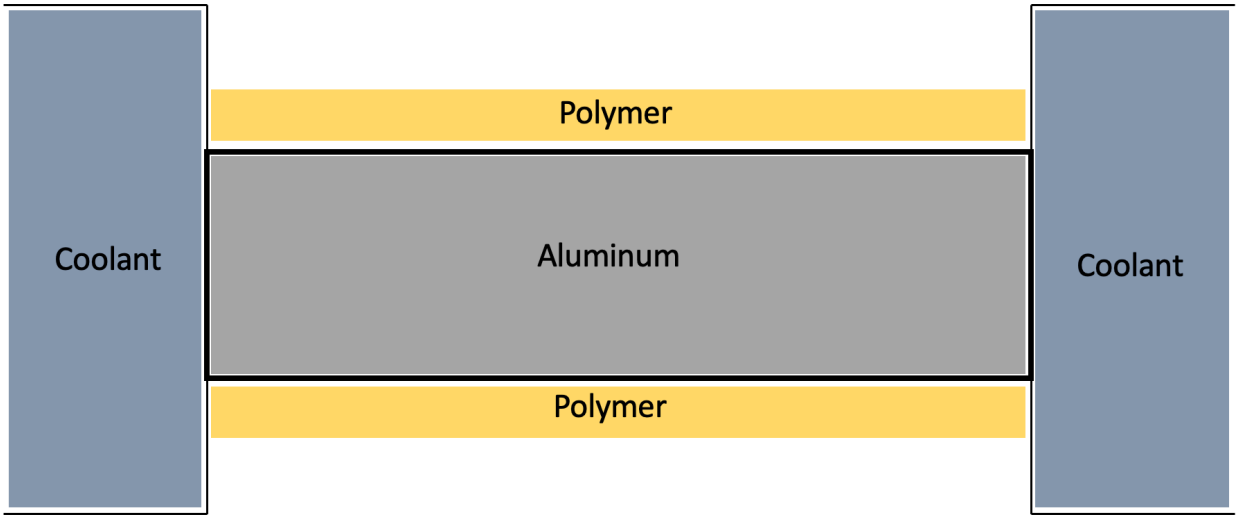


***Figure 20. Aluminum Fin with Polymer Coating***

Considering only the aluminum and using symmetry, the system can be simplified to:

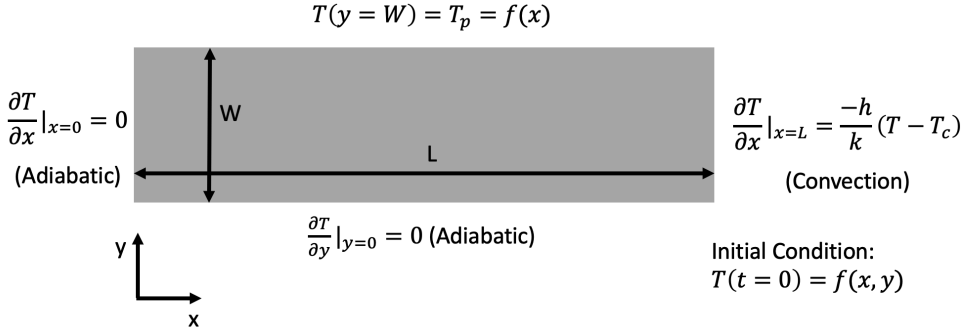


***Figure 21. Simplified Aluminum Fin with Boundary Conditions and Initial Condition. The boundary condition at the top surface represents the contact with the polymer, where the temperature of the aluminum will be equal to the temperature of the polymer, which can be represented as a function of position.***

Using the method of superposition, this transient, non-homogeneous problem can be reduced to several, more simple problems with solutions that can be recombined to obtain the total temperature distribution.

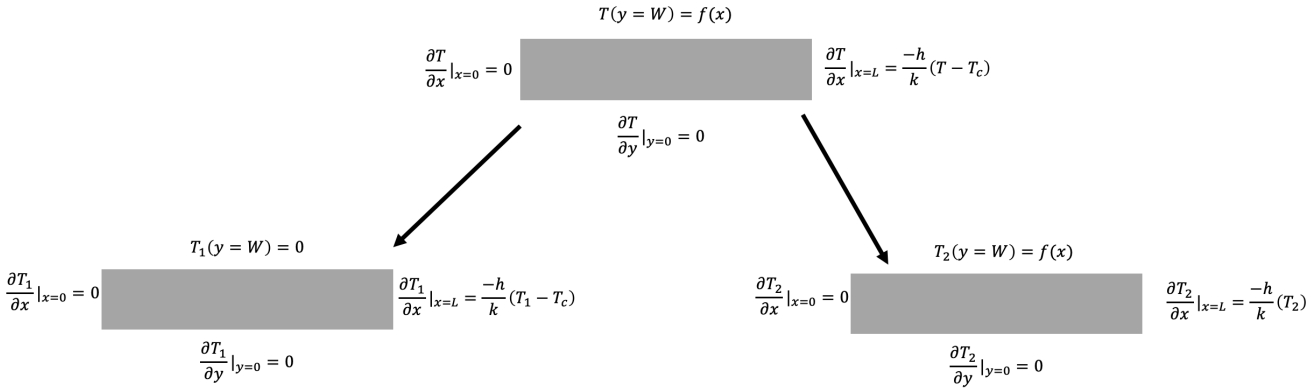


***Figure 22. Steady State Problem***

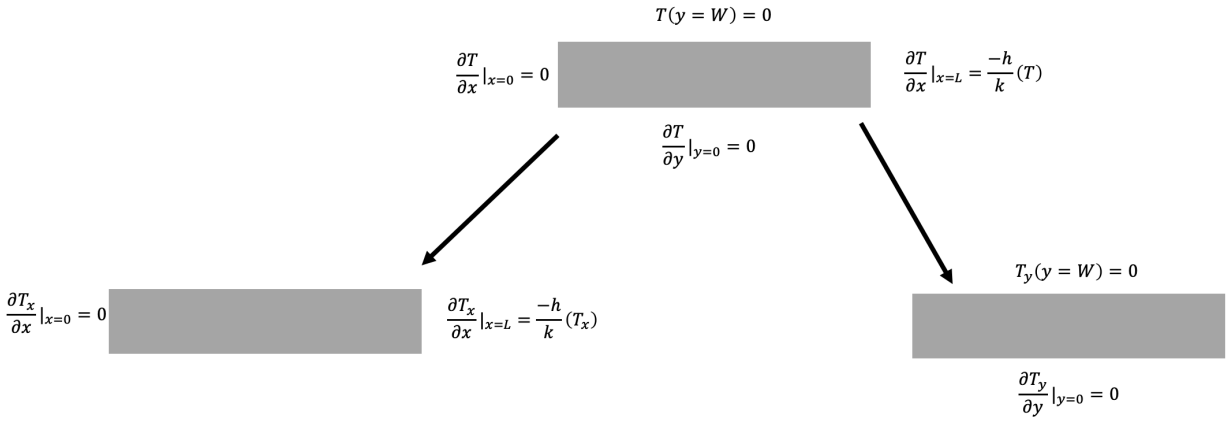


***Figure 23. Transient Problem***

This process can then be repeated for the polymer film coating and for different steps in the process, boundary conditions, or assumptions about the system. These equations can then converted to a MATLAB script that obtains the temperature distribution for the system. This numerical model, using an iterative solutions and the first several terms of the infinite series solutions, is very close to completion. Using the temperature distribution, analysis deriving from the first and second laws of thermodynamics, and input parameters based on system geometry and material properties, a wide range of system configurations can be studied, allowing this system to be optimized for maximum efficiency and performance.

## ii.d. Novel inorganic thermal conductivity switching material using voltage and heat as external stimuli

A promising class of material candidates for dynamic thermal conductivity switching that has recently received considerable attention due to their fast, repeatable, and well-integrated trigger mechanism are ferroelectric (FE) perovskites, such as lead zirconate titanate PZT and lead titanate PTO. In these FE materials, the application of a sufficiently large electric field alters the ferroelectric domain structure and the corresponding domain-wall population densities. The thermal conductivity of these FE solids is dominated by phonons, and any variations in their domain-wall density could potentially impact their scattering rate and change their thermal conductivity. Despite the large focus on investigating the thermal conductivity of PZT under varying conditions, its antiferroelectric (AFE) end-member, lead zirconate PZO has received much less attention. In this material, a sufficient electric field will transition the antiferroelectric phase to a ferroelectric phase, where there is a volume expansion, reduction in the unit-cell size from 8 formula units to 6, and the possibility of altering the populations of ferroelastic domains. Furthermore, these ferroelastic domains within antiferroelectric PZO may directly impact phonon scattering rates. In addition to the AFE-to-FE phase transition, PZO undergoes another phase transition upon heating, transitioning from antiferroelectric to paraelectric (PE), where the lattice structure goes from 8 formula units to 1, and thus can be expected to reduce the phonon scattering rate and lead to higher thermal conductivities.

The application of PZO in functional devices relies heavily on the ability to maintain and regulate the material's temperature; for example, both the pyroelectric and electrocaloric efficiency of PZO are highly temperature-sensitive quantities. As part of this program, we have demonstrated how the thermal conductivity of an antiferroelectric solid, PZO, can be bidirectionally switched between low- and high-thermal conductivities using electrical and thermal excitation, respectively. We show that the thermal conductivity of PZO decreases by 10% via domain restructuring during electrical biasing and can be increased by up to 25% upon heating; the combination of these mechanisms allows for thermal conductivity switching of ~38%, which is significantly larger than previously reported switching in PZT and PTO.

Specifically, we demonstrated how electric fields and thermal effects can be used in tandem to create a bidirectional thermal conductivity switch. For this, we periodically apply electrical and optical excitation to the 60-nm-thick epitaxial PZO sample and switch the material between low- and high-thermal conductivity states. Figure 1a and b show the switching mechanism in real-time when the PZO is under periodic electric field and heating, respectively. For an electric field amplitude of 670 kV $cm^{-1}$ the thermal conductivity can be periodically decreased by nearly 10%. On the other hand, upon applying optical heating using a laser with a spot size of 12 μm in diameter, the PZO thermal conductivity increases by nearly 25%. Figure 1c and d show this transition is repeatable for a number of cycles. Although switching thermal conductivity using electric field shows some drift from one cycle to another, we attribute this to the existence of a small sensitivity to the film thermal conductivity rather than inherent changes in the film due to cycling or due to different domain structures upon each field cycle. On the other

hand, we observe a small decay in thermal conductivity of PZO as well as reflectivity signal after multiple switching cycles with the laser source, which is attributed to gradual degradation in the SRO transducer due to heating cycles.

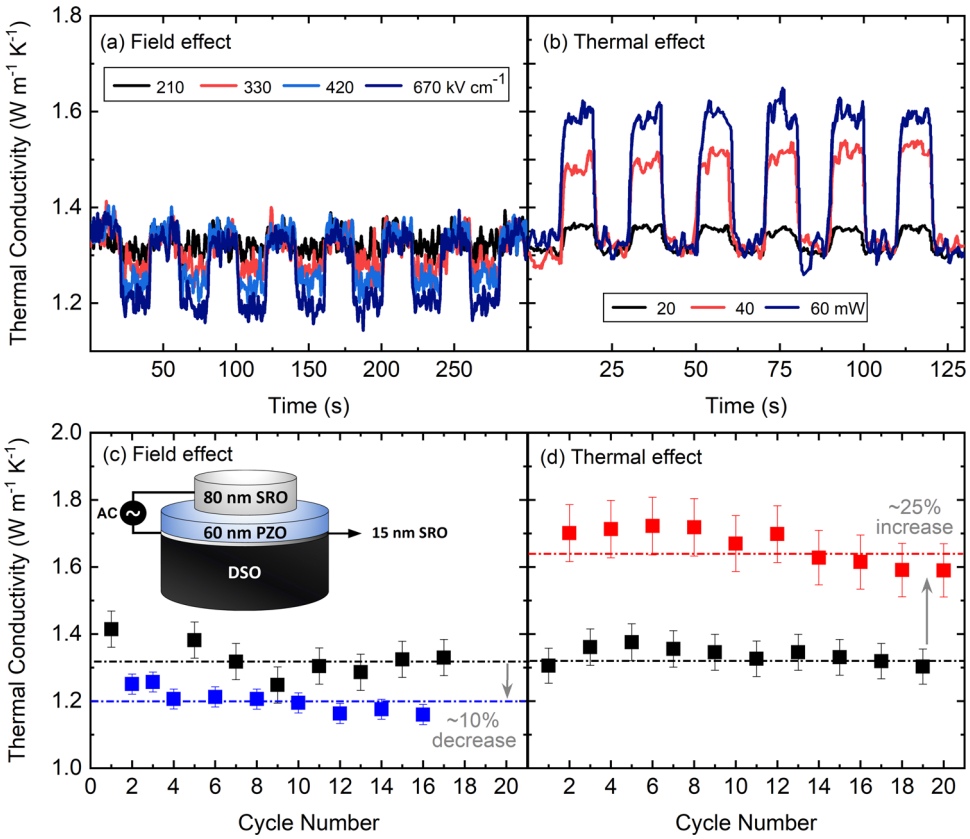


***Figure 24. Real-time switching of epitaxial PZO to low and high thermal conductivity using electrical and thermal stimuli. Switching thermal conductivity of PZO as a function of time measured at 500 ps delay time for (a) electric fields of 210, 330, 420, and 670 kV cm$^{-1}$, and (b) heater laser powers of 20, 40, and 60 mW. (c, d) Repeatability of switching thermal conductivity upon applying maximum electric field and laser power before damaging the sample. The dashed lines represent the weighted average of the data points corresponding to that line. These measurements were performed at a single location on the sample. The uncertainty is calculated based on a 10% change in transducer thickness.***

In summary, we demonstrated the thermal conductivity of antiferroelectric PZO can be bidirectionally switched by −10% and +25% upon application of electric field and thermal excitation, respectively. Similar to ferroelectric materials where the application of electric field increases the domain-wall density and reduces the thermal conductivity, we observe that the thermal conductivity of antiferroelectric PZO decreases upon applying an electrical bias across the sample. Furthermore, we take advantage of PZO's relatively low Curie temperature (220 °C) and, using optical heating, we induce the orthorhombic to cubic phase transition, resulting in higher crystal symmetry and increased thermal conductivity in PZO. According to our results, the net thermal conductivity switching ratio that can be obtained in PZO is around 38%.